



# 1 Vertical profiling and aerosol typing using fluorescence Raman and 2 depolarization lidar measurements over Thessaloniki, Greece

3 Georgia Peletidou<sup>1</sup>, Kalliopi A. Voudouri<sup>1,2</sup>, Konstantinos Michailidis<sup>1</sup>, Peristera Paschou<sup>2</sup>, Nikolaos  
4 Siomos<sup>3</sup>, Jens Reichard<sup>4</sup>, and Dimitrios Balis<sup>1</sup>

5 <sup>1</sup>Aristotle University of Thessaloniki, Department of Physics, 54124 Thessaloniki, Greece

6 <sup>2</sup>National Observatory of Athens, Institute for Astronomy, Astrophysics, Space Applications and Remote Sensing, 15236  
7 Athens, Greece

8 <sup>3</sup>Chair of Experimental Meteorology, Faculty of Physics, Ludwig-Maximilians-Universität München, 80539 München,  
9 Germany

10 <sup>4</sup>Richard-Aßmann-Observatorium, Deutscher Wetterdienst, Lindenberg, Germany

11

12 *Correspondence to:* Georgia Peletidou ([gpeletid@auth.gr](mailto:gpeletid@auth.gr)) —

13 **Abstract.** In this study, we present the first fluorescence lidar observations over Thessaloniki, Greece, (40.63°N, 22.96°E;  
14 60m a.s.l.) using a multiwavelength Raman and depolarization lidar with fluorescence capabilities. For the first time in the  
15 Eastern Mediterranean fluorescence backscattering coefficient and the spectral fluorescence capacity parameter are retrieved  
16 and combined with particle depolarization ratio, lidar ratios, and Ångström exponents to characterize the aerosol load over  
17 Thessaloniki, a region influenced by diverse aerosol sources. Representative case studies of biomass-burning smoke, Saharan  
18 dust, and mixed pollen event showing distinct fluorescence properties are discussed in detail, while an extended dataset  
19 covering the period April 2024 - December 2025 is further analysed, comprising 108 aerosol layers from 50 measurement  
20 cases. A sub-dataset is also compared with the EARLINET Mahalanobis distance-based typing algorithm, highlighting the  
21 importance and complementarity of fluorescence lidar observations on the aerosol characterization in complex environments.  
22 Based on the spectral fluorescence capacity and the particle depolarization ratio, the identified layers are classified into smoke,  
23 dust, polluted continental, clean continental and mixed pollen. THELISYS retrievals show that the spectral fluorescence  
24 capacity depends on aerosol type, with smoke showing the highest values ( $3.5 \times 10^{-6} - 12.7 \times 10^{-6} \text{ nm}^{-1}$ ), followed by  
25 mixed pollen ( $2.3 \times 10^{-6} - 4.8 \times 10^{-6} \text{ nm}^{-1}$ ), polluted continental ( $1.0 \times 10^{-6} - 3.3 \times 10^{-6} \text{ nm}^{-1}$ ), clean continental  
26 ( $0.3 \times 10^{-6} - 1.2 \times 10^{-6} \text{ nm}^{-1}$ ) and dust ( $0.6 \times 10^{-6} - 1.3 \times 10^{-6} \text{ nm}^{-1}$ ). The fluorescence capacity values observed for  
27 all aerosol types are comparable with other studies across central and northern Europe, however the linear particle  
28 depolarization ratio measurements attributed to pollen differ from those reported at more northern latitudes, possibly reflecting  
29 differences in pollen type.

30



## 31 **1 Introduction**

32 Atmospheric aerosols play a crucial role in Earth's climate system, air quality, and public health. Conventional lidar techniques,  
33 including elastic backscatter, Raman, depolarization, and high-spectral-resolution lidar (HSRL), provide information on  
34 aerosol optical properties, shape, size distributions, and concentrations (Klett, 1981; Fernald, 1984; Ansmann et. al., 1990;  
35 Sassen, 2005; Whiteman, 2003; Burton et. al., 2015). However, these methods lack the sensitivity required for reliable  
36 discrimination among biologically derived particles. Over the past decade, fluorescence lidar has emerged as a powerful  
37 complementary technique, enabling the detection of biochemical constituents and fluorescence properties of aerosols and  
38 thereby enhancing aerosol classification capabilities.

39 Early applications of fluorescence lidar were primarily focused on environmental monitoring, including vegetation  
40 characterization, water quality assessment, and geosphere studies, as summarized by Saito et al. (2018). Since approximately  
41 2014, fluorescence lidar has increasingly been applied to atmospheric research. Two principal approaches for aerosol  
42 fluorescence retrieval have been established, the spectrometric fluorescence lidar and the single channel fluorescence detection  
43 implemented within Mie-Raman lidar systems.

44 In the context of aerosol fluorescence spectroscopy, Reichardt (2014) integrated a multi-channel fluorescence spectrometer  
45 into a standard Raman lidar system, enabling the first quantitative retrievals of aerosol fluorescence. This methodology was  
46 subsequently refined through improved calibration and retrieval techniques (Reichardt et al., 2023) and extended to a multi-  
47 year dataset (2020–2023) that could only be obtained by spectrometric measurements (Reichardt et al., 2023b; 2025). A key  
48 outcome of these studies was the introduction of the spectrum of fluorescence capacity and the connections between aerosol  
49 fluorescence and other parameters and influencing factors, such as the elastic-optical particle properties, the type and origin of  
50 the aerosols, the atmospheric state variables, and clouds.

51 In parallel, Veselovskii et al. (2020) extended the operational capabilities of lidar, compatible with systems that are in  
52 accordance with the Aerosol, Clouds and Trace Gases Research Infrastructure (ACTRIS; <https://www.actris.eu/>) for Aerosol  
53 Remote Sensing requirements. Their approach involved the integration of a single broadband fluorescence channel centered  
54 at 466 nm into the multiwavelength Mie–Raman lidar system LILAS. Initial feasibility studies conducted between 2018 and  
55 2020 demonstrated that even a single fluorescence channel allows for the retrieval of fluorescence backscattering coefficients  
56 and the derivation of an intensive fluorescence capacity parameter.

57 The standardisation of quantitative particle fluorescence retrievals into operational lidar systems represents a major challenge  
58 in aerosol classification using remote sensing. By combining fluorescence capacity with particle depolarization ratio, intensive  
59 aerosol classification has been achieved (Veselovskii et al., 2022b; 2025). Veselovskii et al. (2021, 2022a, 2023) demonstrated  
60 discrimination among pollen, biomass-burning smoke, mineral dust, urban aerosols, and cirrus clouds with high spatial and  
61 temporal resolution. These studies conducted over Lille revealed that smoke layers transported from North America exhibited  
62 fluorescence capacities up to an order of magnitude higher than urban aerosols, while Saharan dust was characterized by low  
63 fluorescence capacity but high depolarization ratios. Pollen events were identified by concurrent enhancements in both



64 depolarization and fluorescence capacity, frequently forming mixed layers with urban aerosols within the planetary boundary  
65 layer. Furthermore, Hu et al. (2022) extended this methodology to complex atmospheric scenarios involving overlapping  
66 smoke and cirrus layers, demonstrating that fluorescence based classification remains useful even under cloud-contaminated  
67 conditions. More recently, Gast et al. (2025) validated the general applicability of this approach by demonstrating consistent  
68 aerosol classification across different lidar systems and geographic regions.

69 Collectively, these studies demonstrate that fluorescence based aerosol classification enhances aerosol typing, particularly  
70 under conditions where traditional multiwavelength Mie–Raman approaches encounter limitations. This capability provides a  
71 powerful tool for atmospheric monitoring and for advancing the understanding of aerosol–cloud interactions (Reichardt, 2014;  
72 Reichardt et al., 2018). In this context, aerosol typing over Thessaloniki during the period 2024–2025 represents a particularly  
73 valuable case study. Thessaloniki is a densely populated urban site in the Eastern Mediterranean, where mineral dust, biomass-  
74 burning smoke, anthropogenic pollution, pollen and marine aerosols frequently coexist, rendering it an ideal location for  
75 evaluating and refining aerosol classification methodologies (Voudouri et al., 2020).

76 Beyond mineral and anthropogenic particles, biological aerosols, especially pollen, constitute a significant yet still  
77 insufficiently characterized fraction of atmospheric aerosols. Extensive research has investigated various aspects of airborne  
78 pollen in Thessaloniki (Papadogiannaki et al., 2025; Vokou et al., 2024; Paschalidou et al., 2020; Charalampopoulos et al.,  
79 2021). Based on long-term observations of 16 pollen taxa, the local pollen spectrum is dominated by Cupressaceae (24.9%),  
80 Quercus (20.8%), Parietaria (13.6%), Olea (9.1%), Pinaceae (8.9%), and Poaceae (6.3%) (Gioulekas et al., 2004). Building on  
81 these findings, Damialis et al. (2007) analysed long-term pollen trends (1987–2005), revealing a general doubling of airborne  
82 pollen concentrations per decade across several taxa. Furthermore, Damialis et al. (2017) conducted one of the few vertical  
83 profiling studies in the region using ground based and airborne platforms, confirming the presence of pollen—particularly  
84 Pinaceae and Quercus—at altitudes up to 2 km above ground level. These observations indicate that pollen grains can remain  
85 airborne for extended periods and undergo long-range transport, thereby expanding the spatial scale of human exposure. Such  
86 findings underscore the need for continuous, high-resolution vertical profiling techniques. In this regard, fluorescence lidar  
87 provides a unique capability for investigating the vertical distribution of pollen by exploiting their intrinsic fluorescent  
88 properties to distinguish biological from non-biological aerosols.

89 Within this framework, the present study reports, for the first time, vertical measurements of aerosol and pollen over  
90 Thessaloniki during 2024–2025, using fluorescence lidar observations in a complex urban Mediterranean environment. The  
91 paper is organized as follows: Sect. 2 describes the lidar system and the analysis methodology, including system configuration,  
92 data pre-processing, and fluorescence retrieval techniques with different interference filters (IF). Sect. 3 presents and discusses  
93 the results of three case studies and the classification scheme based on fluorescence capacity and particle depolarization ratio,  
94 while Sect. 4 summarizes the main conclusions of the study.



## 95 2 Instrument and methods

### 96 2.1 Thessaloniki's lidar system upgrade

97 Thessaloniki's lidar system (THELISYS) is part of the multitype ground-based instruments that belong to the Laboratory of  
98 Atmospheric Physics (LAP), located in the Physics Department of the Aristotle University of Thessaloniki (AUTH), Greece  
99 (40.63°N, 22.96°E; 60m a.s.l.) and is part of the European Aerosol Research Lidar Network (EARLINET:  
100 <https://www.earlinet.org/>). Quality assurance procedures for lidar signals are guaranteed using the Automated Lidar Analysis  
101 Software (ATLAS; <https://github.com/nikolaos-siomos/ATLAS/releases/tag/v0.5.0> ) passing all the quality assurance  
102 standards established within EARLINET (Freudenthaler et al., 2018), providing quality assured aerosol products.

103 THELISYS lidar has been gradually upgraded since 2021, to be fully automated, providing continuous measurements of  
104 aerosol and cirrus cloud properties in the frame of the project “Panhellenic infrastructure for Atmospheric Composition and  
105 climate change” (PANACEA; <https://panacea-ri.gr>). More details about the THELISYS setups through the last decades can be  
106 found in previous studies (Siomos et. al., 2018; Voudouri et. al., 2020; Michailidis, 2023).

107 THELISYS is a  $3\beta+2\alpha+1\delta+1wv+1G$  lidar system that retrieves the aerosol backscatter coefficient ( $\beta_{\text{aer}}$ ) at 3 wavelengths (355,  
108 532, 1064 nm), the aerosol fluorescence backscatter coefficient ( $\beta_{\text{F}}$ ) at 466 nm (since February 2025), the aerosol extinction  
109 coefficient ( $\alpha_{\text{aer}}$ ) at 2 wavelengths (355, 532 nm), alongside aerosol extensive and intensive properties such as backscatter- and  
110 extinction-related Ångström exponents ( $\text{BAE}_{355/532}$ ,  $\text{EAE}_{355/532}$ ,  $\text{BAE}_{532/1064}$ ), lidar ratio ( $\text{LR}_{532}$ ,  $\text{LR}_{355}$ ), volume and particle  
111 linear depolarization ratio ( $\text{VLDR}_{532}$ ,  $\text{PLDR}_{532}$ ), water vapor mixing ratio ( $\text{MR}_{408}$ ) and fluorescence capacity ( $G_{\text{F}}$ ). All collected  
112 signals undergo processing for the retrieval of the lidar profiles using the Single Calculus Chain (SCC; D'Amico et. al., 2015)  
113 algorithm, the fully automated algorithm, which has been developed to provide a common lidar processing tool, within  
114 EARLINET stations. However, SCC in its current version does not handle water vapor and fluorescence channels so for the  
115 new products the signals undergo processing using the in-house Semi-automated multiwavelength Lidar Algorithm (SULA;  
116 Paschou et al., 2022) developed by National Observatory of Athens (NOA) with contribution from AUTH on the water vapor  
117 and fluorescence retrievals.

118 More specifically about the latest upgrades, in June 2023, THELISYS was equipped with a single dual-use channel, one  
119 centered at 470 nm for deriving the aerosol fluorescence capacity similar with the lidar system LIF (Gidakou et. al., 2026)  
120 and the other one centered at 408 nm for deriving the water vapor mixing ratio profile using appropriate IFs. In February 2025,  
121 the IF centered at 470 nm with full width at half maximum (FWHM) of 100 nm in the fluorescence channel was replaced by  
122 an IF at 466 nm with 44 nm FWHM, in order to ensure comparability with lidar systems operating in Lille (Veselovskii et al.,  
123 2021) and Leipzig (Gast et al., 2025). Differences in retrievals arising from the use of different filters can be adjusted as  
124 described in Sect. 2.3. The two IF are resided in a single photomultiplier tube (PMT) that employs a motorized shutter to insert  
125 the appropriate IF whenever we intend to acquire water vapor or fluorescence measurements.

126

127 **Table 1. Technical characteristics of the optical components for the water vapor and fluorescence interference filters of THELISYS.**



Center Wavelength (nm)	408nm	470nm	466nm
Full Width at Half Maximum (nm)	1	100	50
Peak Transmission (%)	>80	>98	>98

128

## 129 2.2 Fluorescence measurements and analysis

130 In this study, the aerosol fluorescence backscatter coefficient and fluorescence capacity were retrieved using the method  
 131 described by Veselovskii et al. (2020). The method relies on the fluorescence signal  $P_F$  and the nitrogen Raman signal  $P_R$ ,  
 132 which are described by the following equations:

$$133 P_F(z) = C_F \beta_F(z) T_L(z) T_F(z) \quad (1)$$

$$134 P_R(z) = C_R \beta_R(z) T_L(z) T_R(z), \quad (2)$$

135 where  $C$  represents the calibration constants,  $\beta$  the backscatter coefficients and  $T$  the atmospheric transmission terms. The  
 136 subscript F, R and L denote fluorescence, nitrogen Raman and elastic scattering, respectively.

137 The ratio of the Eq. (1) to the Eq. (2) is used to obtain the aerosol fluorescence backscatter coefficient  $\beta_F(z)$ :

$$138 \beta_F(z) = \frac{C_R P_F(z)}{C_F P_R(z)} N_R(z) \sigma_R \frac{T_R(z)}{T_F(z)}, \quad (3)$$

139 where  $\sigma_R = 2.744 \times 10^{-30} \text{ cm}^2 \text{ sr}^{-1}$  (Venable et al., 2011) is the vibrational-rotational Raman differential backscattering  
 140 cross section of molecular nitrogen at 355 nm and the number density of nitrogen is given by the relation:

$$141 N_R(z) = c_{N_2} N_{mol}(z) = 0.78 N_{mol}, \quad (4)$$

142 where  $c_{N_2}$  is the volume fraction of nitrogen in air and  $N_{mol}$  is the molecular number density of air for a given temperature  
 143 and pressure, considering the compressibility of air. The ratio  $T_R(z)/T_F(z)$  of the atmospheric transmissions at the Raman and  
 144 fluorescence wavelengths is calculated from the extinction coefficients at the corresponding wavelengths applying the related  
 145 extinction Angstrom exponent correlation,  $EAE_{355/532}$  (Ansmann et al., 1990). The calibration constants  $C_F$  and  $C_R$  are range-  
 146 independent system constants accounting for the overall optical and electronic response of the fluorescence and Raman  
 147 detection channels, respectively. They include contributions from the optical throughput, IF transmission, different PMT  
 148 sensitivity, detector efficiency, and electronic gain of each channel. The calibration factors ratio  $C_R/C_F$  therefore represents  
 149 the relative calibration factor between the Raman and fluorescence channels; it corrects for their different instrumental  
 150 efficiencies and is calculated following the calibration procedure described by Veselovskii et. al. (2020b) and analysed by Gast  
 151 et. al. (2025). This procedure is based on the ratio of the electronic gains of the PMTs and considers each component in the  
 152 respective detection path of the two channels, as described above, thus the calibration factor is given by the relationship:

$$153 \frac{C_R}{C_F} = \frac{g_R T_{IF,R}}{g_F T_{IF,F}}. \quad (5)$$

154 The electronic gain ( $g$ ) was obtained by exchanging the PMTs of the two channels without changing the IF and calculating the  
 155 ratio of the mean signals measured by both PMTs for the fluorescence or the Raman channel. The test produced a PMT gain



156 ratio ( $g_R/g_F$ ) of 1.63. Considering the transmission of the different IFs of the channels ( $T_{IF,R}/T_{IF,F} \sim 0.75$ ) one obtains a value  
157 of  $\sim 1.59$  for  $C_R/C_F$ , the ratio of the calibration factors.

158 Once the fluorescence backscatter coefficient is derived, the fluorescence capacity  $G_F$  can be calculated using the ratio of the  
159 fluorescence backscatter to the aerosol backscatter coefficient at 532 nm retrieved with the Raman backscatter method (Ferrare  
160 et. al., 1998):

$$161 \quad G_F = \frac{\beta_F}{\beta_{532}}. \quad (6)$$

162 Although fluorescence is excited at 355 nm and it would therefore be preferable to use the aerosol backscatter coefficient at  
163 the same wavelength ( $\beta_{355}$ ), the elastic aerosol backscatter coefficient at 532 nm is used here in order to enable comparison  
164 with existing literature.

165 For improved intercomparison with other fluorescence lidar configurations, particularly lidar systems employing broadband  
166 fluorescence channels with varying filter widths or spectrometers, we convert the retrieved fluorescence capacity to a spectral  
167 quantity. The spectral fluorescence capacity  $G_{SF}$  is calculated according to Gast et al. (2025) as

$$168 \quad G_F^{355} = \frac{\beta_F}{\beta_{355} d_{IF}}, \quad (7)$$

169 with  $d_{IF}$  representing the effective bandwidth of the fluorescence IF. Both spectral fluorescence capacity ( $G_F^{355}$ ) and  
170 fluorescence capacity ( $G_F$ ) are presented in the results below to allow comparison with the existing literature. In the text,  $G_F$  is  
171 given in parentheses.

### 172 **2.3 Comparison of different fluorescence interference filters**

173 In lidar instruments that deploy broadband fluorescence channels, the characteristics of the IFs that are being used, such as the  
174 central wavelength and the FWHM, are selected according to the fluorescence emission spectrum of the fluorescing particles  
175 of interest. The particle fluorescence spectrum depends both on the excitation laser line (here 355 nm) and on the particle  
176 chemical composition and mixing state. For an excitation with the 355 (more precisely 354.71 nm) line, an IF with central  
177 wavelength between 466 to 470 nm and bandwidths ranging up to 100 nm has been preferred for broadband fluorescence  
178 applications. Although not necessarily located at the maximum of the fluorescence spectrum, the spectral region 415 – 525 nm  
179 avoids contamination of other major Nd:Yag-related and Raman lines such as the water vapor Raman line at 408 nm and the  
180 2<sup>nd</sup> Nd:Yag laser harmonic at 532 nm and its Anti-Stokes purely rotational Raman band. In THELISYS, an IF centered at  
181 469.55 nm (approximately 470 nm) with 100 nm FWHM was initially deployed to isolate part of the fluorescence spectrum.  
182 However, differences in the IF transmission hindered direct comparison with fluorescence measurements performed in Lille  
183 (Veselovskii et al., 2021) and Leipzig (Gast et al., 2025). In addition, Reichardt et al. (2023) and Veselovskii et al. (2023)  
184 reported that the 424.4 nm second-order vibrational Raman line of N<sub>2</sub> can introduce biases to the fluorescence spectrum  
185 (Reichardt et al., 2023). To improve the consistency of THELISYS lidar with the lidars in Lille and Leipzig, the IF at 470 nm  
186 was replaced by an IF with transmission centered at 465.73 nm (approximately 466 nm) and with 44 nm FWHM. We will refer  
187 to those filters as IF<sub>470,100</sub> and IF<sub>466,44</sub> respectively.



188 The mean  $G_F^{355}$  calculated using such a broad IF will differ from the actual  $G_F^{355}$  at the IF center wavelengths. Using the  $G_F^{355}$   
 189 spectrum measured by Reichardt et al. (2025) as a reference (Fig. 1) we can estimate the systematic relative bias  $\sigma_{G_F,IF_{466}}$  and  
 190  $\sigma_{G_F,IF_{470}}$  of  $G_{F,466}^{355}$  and  $G_{F,470}^{355}$  which are introduced when using IF<sub>466,44</sub> and IF<sub>470,100</sub>, respectively, as

$$191 \sigma_{G_F,IF_{\lambda_0}} = \frac{\overline{G_{F,\lambda_{IF}}^{355}} - G_{F,\lambda_0}^{355}}{G_{F,\lambda_0}^{355}}, \quad (8)$$

192 where  $G_{F,\lambda_0}^{355}$  the spectral fluorescence capacity at  $\lambda_0 = 466$  or  $470$  nm and  $\overline{G_{F,\lambda_{IF}}^{355}}$  is the spectral fluorescence weighted mean  
 193 signal. The latter is calculated using the filter transmission as weighting function:

$$194 \overline{G_{F,\lambda_{IF}}^{355}} = \frac{\int G_F^{355}(\lambda) \times T_{IF}(\lambda) d\lambda}{\int T_{IF}(\lambda) d\lambda}. \quad (9)$$

195

196 **Table 2. Relative systematic bias due to the IF transmission band. Values are calculated relative to the true spectral fluorescence**  
 197 **capacities at 466 and 470 nm which have been taken from Reichardt et al. (2025).**

	$\lambda_{IF}$ (nm)	Lower $\sigma_F$ range (%)	Upper $\sigma_F$ range (%)
$\sigma_{G_F,IF_{466}}$	466	-0.1	1.1
$\sigma_{G_F,IF_{466}}$	470	-0.1	2.8
$\sigma_{G_F,IF_{470}}$	466	-5.5	-2.9
$\sigma_{G_F,IF_{470}}$	470	-6.7	2.9

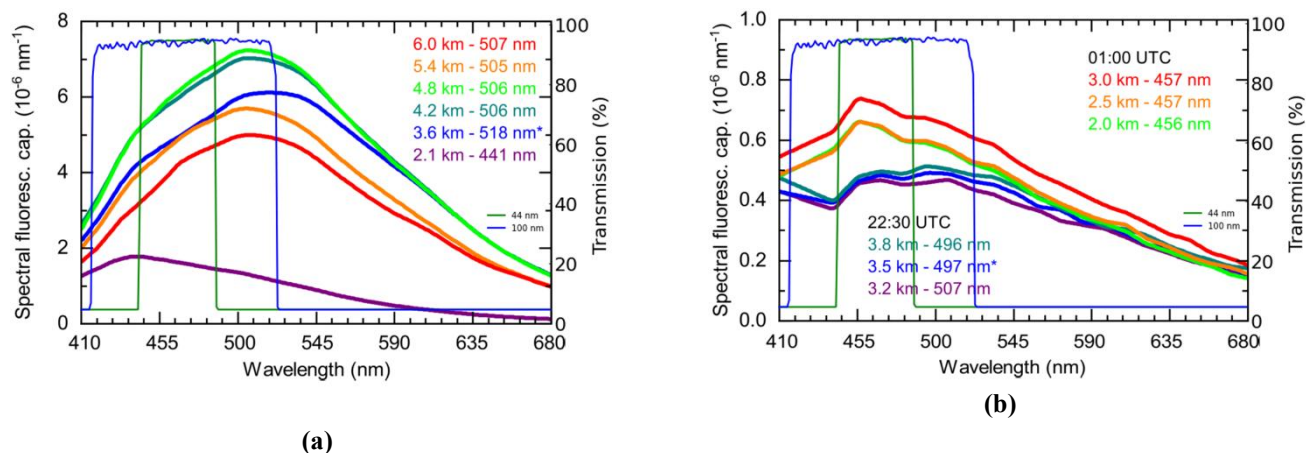
198

199 The values are summarized in Table 2. The lower/upper systematic relative biases correspond to the most negative/positive  
 200 bias calculated from each spectrum of Fig. 1 (including both spectra from biomass burning aerosol and dust). This ensures that  
 201 the error bars are conservative and cover the whole uncertainty range of the dataset displayed in Fig. 1. We see that IF<sub>470,100</sub>  
 202 leads to generally larger biases, even at its central wavelength, with a tendency to underestimate the actual  $G_F^{355}$  value. We  
 203 further compare the biased  $\overline{G_{F,470}^{355}}$  and  $\overline{G_{F,466}^{355}}$  values which occur after transmission through IF<sub>470</sub> and IF<sub>466</sub>, respectively. The  
 204 relative difference between  $\overline{G_{F,470}^{355}}$  and  $\overline{G_{F,466}^{355}}$  with respect to  $\overline{G_{F,466}^{355}}$  is defined as

$$205 \sigma_{\Delta IF} = \frac{\overline{G_{F,470}^{355}} - \overline{G_{F,466}^{355}}}{\overline{G_{F,466}^{355}}}, \quad (10)$$

206 and can range from -5.8 % to 0.6 % for the different spectra of Fig 1.

207



208

209 **Figure 1. Spectral fluorescence capacity measurements of a biomass burning aerosol layer at 22:30 UTC on 4 July 2023 (a) and of a**  
 210 **dust layer at 22:30 and 01:00 UTC in the night of 22–23 February 2021 (b) (Adapted from Reichardt et al., 2025). The blue and**  
 211 **green lines represent the transmission curves of the two THELISYS IFs, illustrating the different fluorescence spectral ranges they**  
 212 **cover.**

213 In order to compare the spectral fluorescence capacity considering the characteristics of IF<sub>466,44</sub> and IF<sub>470,100</sub> we use Eq. 7. The  
 214 IF comparison test was performed on seven separate days in 2025. Here, we present two representative cases: one dominated  
 215 by dust aerosols and another characterized by urban and smoke aerosols, used to compare the two IFs. Table 3 lists the dates  
 216 and times of each measurement.

217

218 **Table 3. Observation dates and UTC time windows for IF<sub>466,44</sub> and IF<sub>470,100</sub> fluorescence measurements**

Date	Time (UTC) IF <sub>466,44</sub>	Time (UTC) IF <sub>470,100</sub>	Aerosol Type
13/03/2025	18:35–20:15	20:17–21:20	Dust
14/05/2025	19:09–20:56	20:58–21:51	Polluted Continental & Smoke

219

220 Across the  $G_F^{355}$ , small differences are observed when comparing the IF<sub>466,44</sub> and the IF<sub>470,100</sub> over Thessaloniki (Fig. 2). For  
 221 instance, on 13 March 2025, an extreme dust event passed over Thessaloniki, providing an opportunity to evaluate the  
 222 performance of the two IFs (Fig. 2a). The aerosol layer was confined within the boundary layer, extending from 0.65 to 3.2  
 223 km.

224

225 **Table 4. Spectral fluorescence capacity mean, minimum and maximum values using the IF<sub>466,44</sub> and the IF<sub>470,100</sub> of the dust layer.**



IF	Mean $G_F^{355}$ ( $10^{-6} \text{ nm}^{-1}$ )	Minimum $G_F^{355}$ ( $10^{-6} \text{ nm}^{-1}$ ) [Altitude (km)]	Maximum $G_F^{355}$ ( $10^{-6} \text{ nm}^{-1}$ ) [Altitude (km)]
IF <sub>466,44</sub>	0.93	0.31 [2.9]	1.24 [1.3]
IF <sub>470,100</sub>	0.86	0.38 [2.8]	1.14 [1.5]

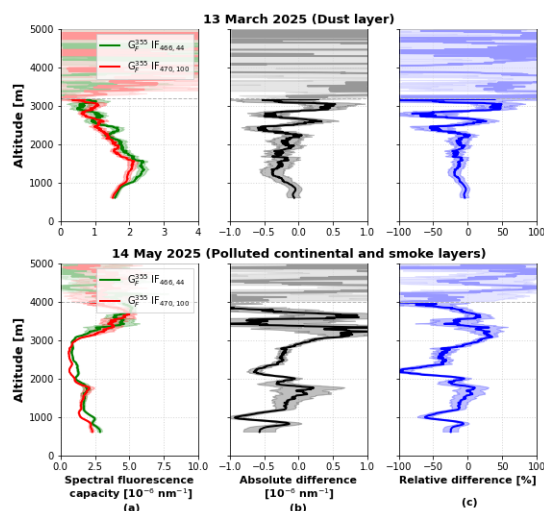
226

227 Applying Eq. (7), we calculated  $G_F^{355}$  using IF<sub>466,44</sub> and  $G_F^{355}$  using IF<sub>470,100</sub>, as shown in Table 4. These results indicate that the  
 228  $G_F^{355}$  retrieved using the two different IFs is comparable and consistent with recent literature (Reichardt et al., 2025) and that  
 229 Eq. (7) provides a useful approach for comparing  $G_F^{355}$  values obtained between different lidar systems. As introduced by  
 230 Reichardt et al. (2025),  $G_F^{355}$  varies with aerosol type, therefore, a second case characterized by urban and smoke aerosols is  
 231 presented in Fig. 2b.

232 Here, the observed differences between  $G_{F,466}^{355}$  and  $G_{F,470}^{355}$  (Fig. 2b, 2c) are much bigger than the systematic error estimation  
 233 due to the IF transmission band especially for shallow layers, and also according to the error bars the noise is too low to explain  
 234 the differences, which leads us to the conclusion that the variations were probably related to atmospheric changes between the  
 235 two measurements as they were not performed simultaneously or iteratively.

236 These findings highlight the importance of standardizing spectral fluorescence capacity within EARLINET to enhance the  
 237 comparability of fluorescence measurements and to improve aerosol characterization and typing schemes.

238



239



240 **Figure 2. (a) Vertical profiles of mean  $G_F^{355}$  for the two cases with subsequent measurements performed both with IF<sub>466,44</sub> (green)**  
241 **and with IF<sub>470,100</sub> (red) filters, (b) absolute difference and (c) relative difference expressed as percentage and normalized to  $G_{F,470}^{355}$**   
242 **on 13 March 2025 (dust layer) and 14 May 2025 (polluted continental and smoke layers). The uncertainties are propagated, assuming**  
243 **random errors using standard Gaussian error propagation.**

### 244 3. Observations and typing of fluorescence measurements

245 Fluorescence measurements have been performed since April 2024 in Thessaloniki. For all these measurements, geometrical  
246 properties (i.e., base, top, and center of mass) of the detected aerosol layers are analysed using the wavelet covariance transform  
247 (WCT) method in signal regions with sufficient signal-to-noise ratio. The WCT method allows the identification of multiple  
248 aerosol layers within a single profile, thus, providing insights into internal layer structure. The WCT method is applied in the  
249 aerosol backscatter coefficient profiles, preferably at 1064 nm since they exhibit stronger vertical gradients and clearer layer  
250 structures than extinction coefficient, particularly at longer wavelengths (Baars et al., 2008; Siomos et al., 2017). A key  
251 parameter in the analysis is the dilation parameter value, as it controls the sensitivity of the method to aerosol structures at  
252 different vertical scales. Larger dilation values highlight major aerosol layers, while smaller values allow the detection of finer  
253 structures. A dilation value of 0.3 km is applied in this study for the detection of lofted aerosol layers to be consistent with  
254 previous studies (e.g. Brooks, 2003; Baars et al., 2008).

255 For each distinct layer, identified by the WCT method, we calculated the mean value of the spectral fluorescence capacity,  
256  $G_F^{355}$ , the particle linear depolarization ratio,  $PLDR_{532}$ , the backscatter related Ångström exponents,  $BAE_{355/532}$  and  
257  $BAE_{355/1064}$ , and the lidar ratios,  $LR_{355}$  and  $LR_{532}$ . The type of each aerosol layer was classified using the EARLINET  
258 Mahalanobis distance-based typing algorithm (EMD), a method specifically developed for the use on the EARLINET database  
259 with a high level of flexibility in order to adapt to the different lidar setups and needs (Papagiannopoulos et al., 2018). The  
260 algorithm applies the Mahalanobis distance classifier (Mahalanobis, 1936) to classify observations into a maximum of eight  
261 (i.e., Dust (D), Volcanic (V), Mixed Dust (MD), Polluted Dust (PD), Clean Continental (CC), Mixed Marine (MM), Polluted  
262 Continental (PC), Smoke (S)) and a minimum of four (i.e., Dust, Maritime, Polluted Smoke, Clean Continental) aerosol classes,  
263 considering the needs of each user and the provided number of the intensive properties. EMD classification has previous been  
264 applied to the Thessaloniki EARLINET dataset during the period 2012–2015 to derive the predominant aerosol type (Voudouri  
265 et al., 2019). The intensive properties that held the most weight among others in the classification and are used in this analysis  
266 are the  $BAE_{355/1064}$ ,  $LR_{532}$ , the ratio of the lidar ratios ( $LR_{532}/LR_{355}$ ) and the  $PLDR_{532}$ .

267 In addition, in order to verify the origin of the detected aerosol layers, we calculated back trajectories by using the HYSPLIT  
268 model (Hybrid Single-Particle Lagrangian Integrated Trajectory; available online:  
269 <https://www.ready.noaa.gov/HYSPLIT.php>, last access: 29 January 2026; Stein et al., 2015). Below, three case studies  
270 involving different types of aerosols and their properties are presented and analysed (Sects. 3.1-3.3). An aerosol classification  
271 approach based on spectral fluorescence capacity is applied to the full THELISYS dataset in Sect. 3.4.1. Finally, fluorescence-



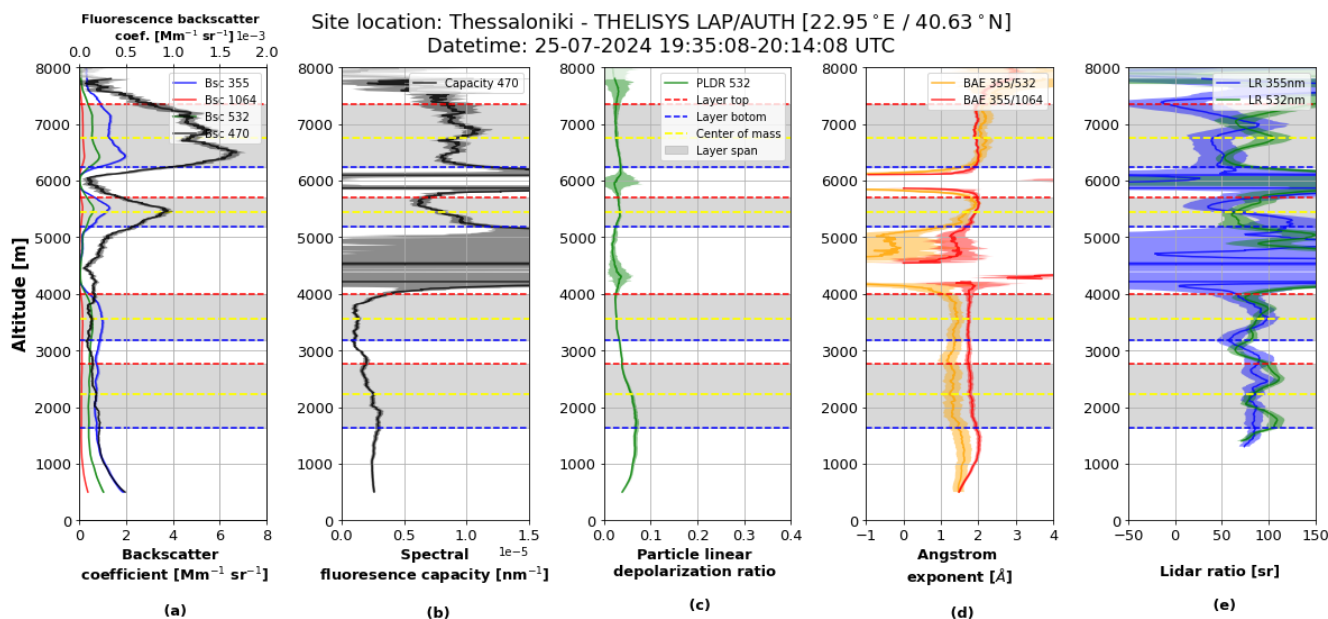
272 based aerosol typing and EMD classification approach are compared, identifying similarities and differences in the detected  
 273 aerosol types and demonstrating the complementary nature of the two methods for aerosol characterization (Sect. 3.4.2).

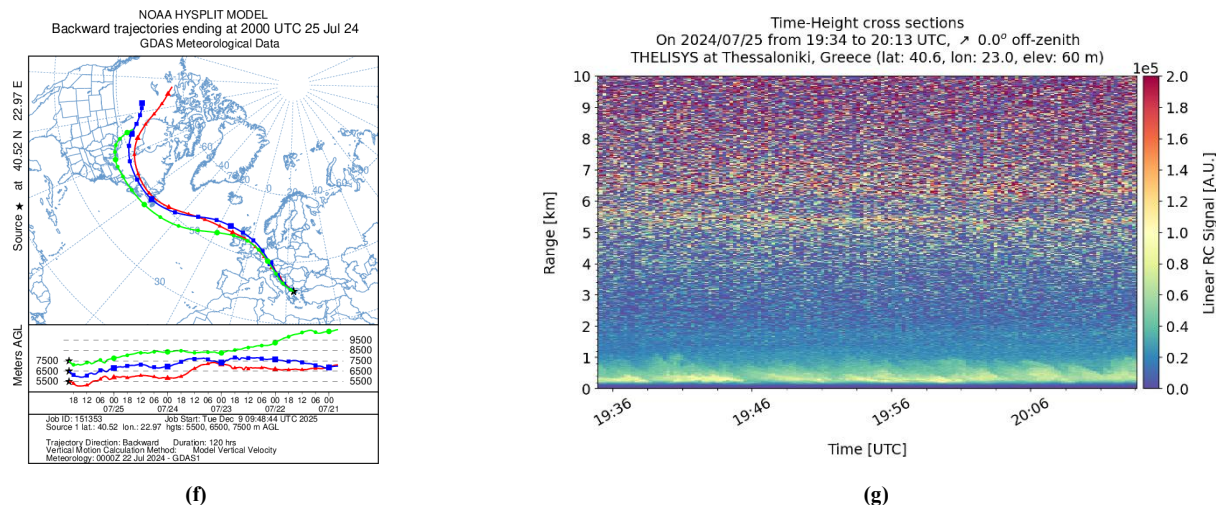
### 274 3.1 Fluorescence properties of a smoke layer

275 During 2024 Canada experienced one of its most severe wildfire seasons. The wildfire activity began in April and persisted  
 276 through June and July, with smoke plumes from these wildfires having undergone episodes of long-range transport across the  
 277 Atlantic, reaching western, central and eastern Europe. THELISYS monitored the smoke layers throughout this period, and  
 278 the case presented in Fig.3 corresponds to a smoke transport event that persisted for six days (22–26 July 2024). The 5-day  
 279 backward trajectories from HYSPLIT (Fig. 3f), in conjunction with fire locations from the MODIS FIRMS product (not shown  
 280 here), confirm that the biomass-burning aerosol was transported from Canada to the region of Thessaloniki.

281 The retrieved profiles of the particle and fluorescence backscatter coefficients, spectral fluorescence capacity, particle  
 282 depolarization ratio, lidar ratios and Angstrom exponents are presented in Fig. 3a-e. Four distinct aerosol layers of different  
 283 aerosol types have been identified; the first two are below 4 km and the other two above 4.8 km.

284





285 **Figure 3. Vertical profiles of the backscatter coefficients (a), spectral fluorescence capacity (b), particle linear depolarization ratio**  
 286 **(c), Angstrom exponents (d), lidar ratios (e), HYSPLIT backward trajectory model (f) and temporal evolution of the range corrected**  
 287 **signal at 470nm (g) on 25 July 2024.**

288

289 **Table 5. Mean values of the aerosol optical properties for the aerosol layers and aerosol type by EMD.**

Layer	Layer base (m)	Layer top (m)	$G_F^{355}$ ( $10^{-6} \text{ nm}^{-1}$ )	PLDR <sub>332</sub>	BAE <sub>355/1064</sub> (Å)	LR <sub>355</sub> (sr)	LR <sub>532</sub> (sr)	EMD
1 <sup>st</sup>	1642	2760	$2.4 \pm 0.2$	$0.05 \pm 0.003$	$1.81 \pm 0.22$	$85.49 \pm 10$	$92.98 \pm 7$	PC
2 <sup>nd</sup>	3195	3997	$1.5 \pm 0.2$	$0.03 \pm 0.001$	$1.74 \pm 0.17$	$81.03 \pm 15$	$86.01 \pm 8$	PC
3 <sup>rd</sup>	4642	5715	$8.2 \pm 0.7$	$0.03 \pm 0.002$	$1.88 \pm 0.77$	$65.52 \pm 22$	$73.52 \pm 15$	PC
4 <sup>th</sup>	6240	7395	$9.1 \pm 0.8$	$0.03 \pm 0.004$	$1.96 \pm 0.45$	$85.99 \pm 32$	$91.15 \pm 17$	S

290

291 The mean values for each layer are summarized in Table 5. Based on numerical values, as well as the corresponding vertical  
 292 distribution, the two lowermost layers exhibit similar mean values of the aerosol optical properties, and their fluorescence  
 293 capacity remains below  $2.5 \times 10^{-6} \text{ nm}^{-1}$ , indicating the presence of similar aerosols. Based on these characteristics, and  
 294 supported by the EMD classification, both layers are identified as polluted continental. In the third layer, although the mean  
 295 values of PLDR, BAE<sub>355/532</sub>, LR<sub>355</sub>, and LR<sub>532</sub>, together with the EMD, again point to a polluted continental aerosol type,  
 296 the mean  $G_F^{355}$  value differs substantially, reaching  $8.2 \times 10^{-6} \text{ nm}^{-1}$  ( $G_F = 5.1 \times 10^{-4}$ ). The increased  $G_F^{355}$  value clearly indicates  
 297 the presence of a different aerosol type in this layer, and, following the findings of Reichardt et. al. (2025) for the spectral  
 298 fluorescence capacity and of Gast et. al. (2025) and Veselovskii et. al. (2022b) for fluorescence capacity, we infer that this  
 299 type corresponds to smoke. Finally, in the third layer, both the mean values of PLDR<sub>532</sub>, BAE<sub>355/532</sub>, LR<sub>355</sub>, LR<sub>532</sub> and  
 300 the EMD, as well as the mean  $G_{SF}$  value,  $9.0 \times 10^{-6} \text{ nm}^{-1}$  ( $G_F = 7.2 \times 10^{-4}$ ), show that this layer corresponds to smoke.

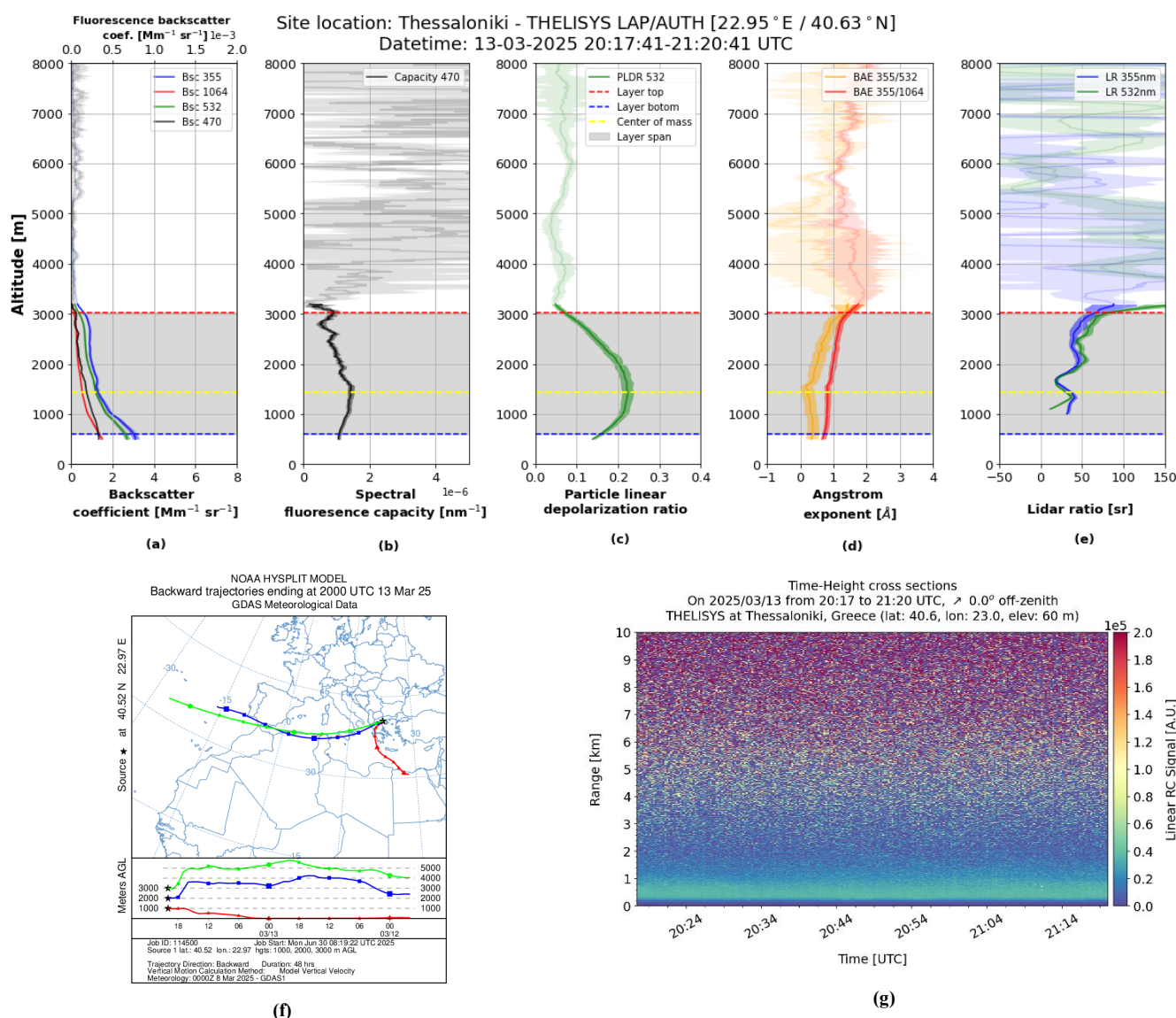


301 **3.2 Fluorescence properties of a dust layer**

302 An extreme dust transport event was monitored by THELISYS in mid-March 2025, lasting six days (11–16 March 2025, Fig.  
 303 4). The 2-day backward trajectory analysis using HYSPLIT, combined with the DREAM8b-CAMS model (Nickovic et. al.,  
 304 2001, not shown), confirms that the detected dust plume originated from the Sahara and was transported to the Thessaloniki  
 305 region (Fig. 4f).

306

307



308 **Figure 4. Vertical profiles of the backscatter coefficients (a), spectral fluorescence capacity (b), particle linear depolarization ratio**  
 309 **(c), Angstrom exponents (d), lidar ratios (e), HYSPLIT backward trajectory model (f) and temporal resolution of the range corrected**



310 **signal at 470nm (g) on 13 March 2025. (Please note that for the spectral fluorescence capacity in panel b an x-axis scaling is employed**  
 311 **which is different from the one used in the other figures.)**

312

313 **Table 6. Mean values of the aerosol optical properties for the dust layer and aerosol type by EMD.**

Layer	Layer base (m)	Layer top (m)	$G_F^{355}$ ( $10^{-6} \text{ nm}^{-1}$ )	PLDR <sub>532</sub>	BAE <sub>355/1064</sub> (Å)	LR <sub>355</sub> (sr)	LR <sub>532</sub> (sr)	EMD
1 <sup>st</sup>	608	3022	$0.92 \pm 0.12$	$0.18 \pm 0.01$	$0.96 \pm 0.19$	$38.75 \pm 4$	$42.96 \pm 3$	D

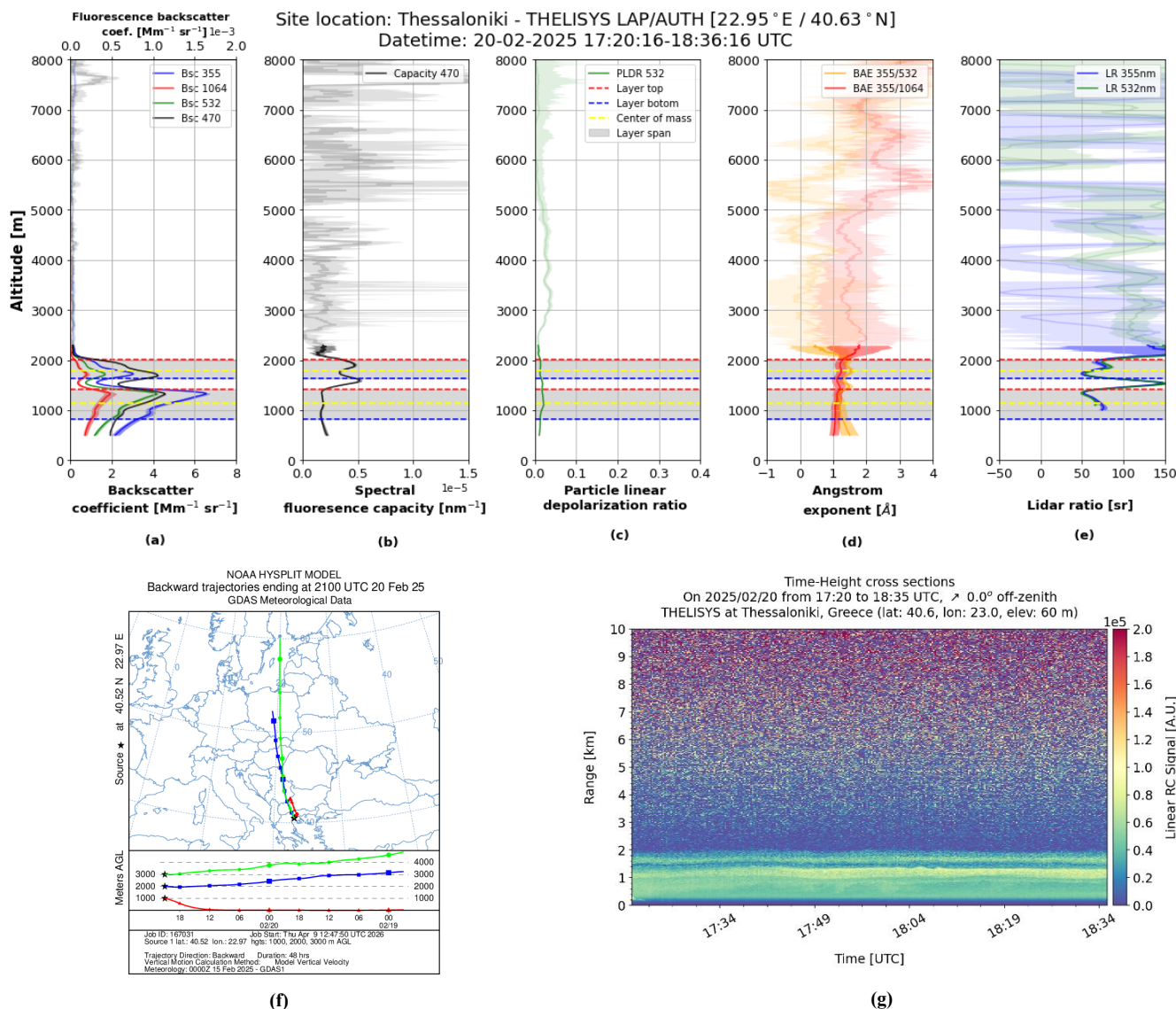
314

315 The retrieved profiles of the particle backscatter coefficients, spectral fluorescence capacity, particle depolarization ratio, lidar  
 316 ratios and Angstrom exponents are shown in Fig. 4a-e. There is one aerosol layer recognized and the mean values for this layer  
 317 are presented in Table 6. The retrieved optical properties values indicate the presence of coarse particles and are consistent  
 318 with the typical dust characteristics observed over Thessaloniki (Siomos et al., 2018; Voudouri et al., 2019). In addition, the  
 319 mean spectral fluorescence capacity  $0.92 \times 10^{-6} \text{ nm}^{-1}$  ( $G_F = 0.59 \times 10^{-4}$ ) is quite low, in agreement with the findings of  
 320 Reichardt et al. (2025) and of Veselovskii et al. (2020) for the fluorescence capacity regarding the presence of dust particles.  
 321 The EMD likewise identifies this layer as dust.

### 322 3.3 Fluorescence properties of a mixed pollen layer

323 Komnos et. al. (2022) findings showed that totally 10 pollen families and two fungi were recognized over Northwestern Greece.  
 324 Damialis et. al. (2007) reported that the taxa with the most abundant pollen atmospheric levels in Thessaloniki were those of  
 325 Cupressaceae, Quercus, Urticaceae, Pinaceae, and Oleaceae; these comprised 72.5% of the total pollen flora. A mixed pollen  
 326 layer was detected by THELISYS on 20 February 2025 (Fig. 5). This observation coincides with the beginning of the pollen  
 327 season in Greece, which generally lasts from February to September (Komnos et al., 2022; Damialis et al., 2007). The back-  
 328 trajectory analysis demonstrates that the air masses in this episode were transported from the Balkans (Fig. 5f).

329



330 **Figure 5. Vertical profiles of the backscatter coefficients (a), spectral fluorescence capacity (b), particle linear depolarization ratio**  
 331 **(c), Angstrom exponents (d), lidar ratios (e), HYSPLIT backward trajectory model (f) and temporal resolution of the range corrected**  
 332 **signal at 470nm (g) on 20 February 2025.**

333

334 **Table 7. Mean values of the aerosol optical properties for the aerosol layers and aerosol type by EMD.**

Layer	Layer base (m)	Layer top (m)	$G_P^{355}$ ( $10^{-6} \text{ nm}^{-1}$ )	PLDR <sub>532</sub>	BAE <sub>355/1064</sub> (Å)	LR <sub>355</sub> (sr)	LR <sub>532</sub> (sr)	EMD
1 <sup>st</sup>	817	1417	$1.8 \pm 0.06$	$0.02 \pm 0.0003$	$1.09 \pm 0.13$	$59.38 \pm 3$	$54.40 \pm 1$	PC



2 <sup>nd</sup>	1635	2002	$4.5 \pm 0.15$	$0.02 \pm 0.0002$	$1.21 \pm 0.08$	$65.83 \pm 4$	$71.41 \pm 2$	PC
-----------------	------	------	----------------	-------------------	-----------------	---------------	---------------	----

335

336 The retrieved vertical profiles of particle backscatter coefficients, spectral fluorescence capacity, particle linear depolarization  
 337 ratio, Ångström exponents and lidar ratio are shown in Fig. 5a–e. Two distinct aerosol layers are identified where the first  
 338 layer extends from 0.8 to 1.4 km and the second from 1.6 to 2 km.

339 The mean values of the optical properties for each layer are shown in Table 7. In the first layer, the mean  $G_F^{355}$  is only  
 340  $1.8 \times 10^{-6} \text{ nm}^{-1}$  ( $G_F = 1.05 \times 10^{-4}$ ), indicating the presence predominantly of polluted continental aerosols. The second layer  
 341 exhibits a higher mean  $G_F^{355}$  equal to  $4.5 \times 10^{-6} \text{ nm}^{-1}$  ( $G_F = 2.3 \times 10^{-4}$ ), a similar PLDR (0.02), and a higher  $BAE_{355/1064}$   
 342 (1.22). The retrieved values in the second atmospheric layer, particularly the high fluorescence capacity observed at this  
 343 altitude, together with the absence of confirmed biomass-burning aerosols on that day, suggest the presence of pollen.  
 344 Veselovskii et al. (2021) reported fluorescence capacity values around  $1.5 \times 10^{-4}$  and particle linear depolarization ratio  
 345 (PLDR) values at 532 nm around 0.1 for pollen, while Filioglou et al. (2023) found higher PLDR values under pollen-  
 346 dominated conditions, approximately 0.28 for birch pollen and 0.43 for pine pollen when background aerosol contributions  
 347 were minimal. In Thessaloniki, lower particle linear depolarization ratio values were retrieved, likely due to the mixing of  
 348 pollen with urban aerosols and/or the presence of different pollen taxa. During the end of February, Cupressaceae pollen is  
 349 present in the atmosphere (Komnos et al., 2022). These pollen grains are almost spherical, with diameters ranging from 15 to  
 350 35  $\mu\text{m}$ , so probably these coarse particles were present in the observed layer.

### 351 3.4 Variability of aerosol types in Thessaloniki

#### 352 3.4.1 Aerosol typing including spectral fluorescence capacity

353 The complete THELISYS dataset for the period between April 2024 and December 2025 is analysed as the cases above. From  
 354 a total of 50 measurements, 108 layers are identified by the WCT method. All layers are located above the full-overlap region  
 355 (i.e., 0.35 km), extending to altitudes exceeding 10 km, indicating the presence of both boundary-layer aerosols and elevated  
 356 layers in the free troposphere.

357 Figure 6a illustrates the individual layers, with colours representing their corresponding  $G_F^{355}$  values. The observed  $G_F^{355}$  values  
 358 span several orders of magnitude, from approximately  $10^{-7}$  to  $10^{-5}$ . As shown, higher values ( $G_F^{355} > 3 \times 10^{-6} \text{ nm}^{-1}$ ) are observed  
 359 during the summer months at mid to high altitudes, particularly between 3 and 8 km, suggesting the presence of strongly  
 360 fluorescent aerosols, commonly associated with biomass-burning smoke transported over long distances. Throughout the year,  
 361  $G_F^{355}$  varies around  $1 \times 10^{-6} \text{ nm}^{-1}$  for aerosol layers residing mainly at low altitudes ( $< 4 \text{ km}$ ), while lower values ( $G_F^{355} < 1 \times 10^{-6}$   
 362  $\text{nm}^{-1}$ ) are observed for some specific dust events, totally clear days and cloudy days.

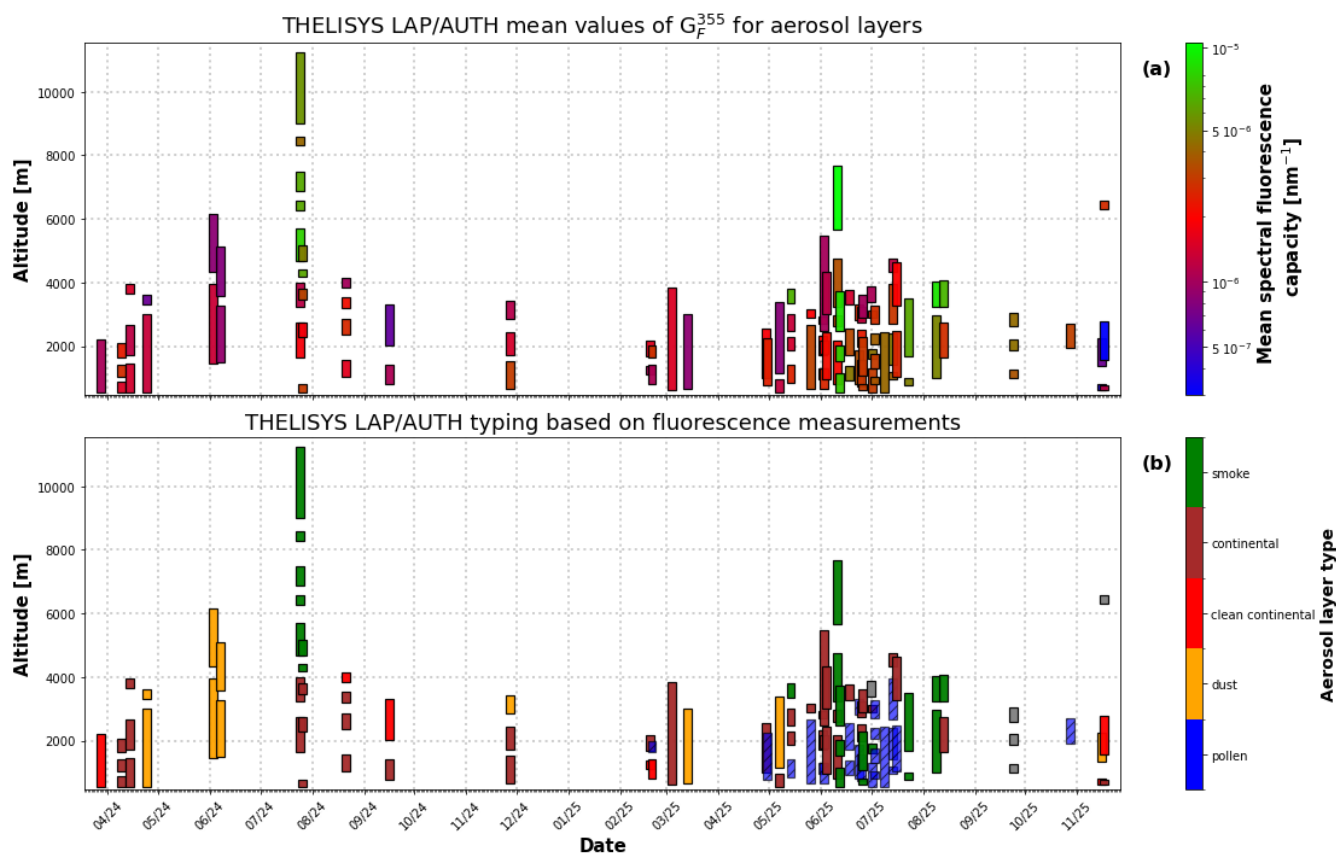
363 The classification of all layers was primarily based on the spectral fluorescence capacity and the particle depolarization ratio.  
 364 For cases where the particle type was not clearly identified from these two parameters, the lidar ratio and backscatter Ångström  
 365 exponent were also considered. In addition, the layer altitude was considered, since at different heights certain aerosols may



366 exhibit similar spectral fluorescence capacity. For example, layers with biomass burning aerosols are typically observed above  
 367 4 km (Michailidis et. al., 2024), whereas transported pollen layers are observed below 2.5 km (Damialis et. al., 2017).  
 368 Furthermore, the maximum layer value of the spectral fluorescence capacity was used to discriminate among clean continental  
 369 ( $0.6 \times 10^{-6} \text{ nm}^{-1} < G_F^{355},_{\text{max}} < 1.8 \times 10^{-6} \text{ nm}^{-1}$ ), polluted continental ( $1.4 \times 10^{-6} \text{ nm}^{-1} < G_F^{355},_{\text{max}} < 3.6 \times 10^{-6} \text{ nm}^{-1}$ ) and mixed pollen  
 370 ( $2.3 \times 10^{-6} \text{ nm}^{-1} < G_F^{355},_{\text{max}} < 6.4 \times 10^{-6} \text{ nm}^{-1}$ ) aerosol. The presence of smoke and dust is further confirmed by the HYSPLIT  
 371 trajectory model, other forecasting models, and satellite observations, as discussed in the two corresponding cases in Sect. 3.1  
 372 and 3.2.

373 Based on the above criteria, Fig. 6b shows the classified aerosol types; smoke (green), dust (orange), continental (brown),  
 374 clean continental (red), mixed pollen (blue). Overall, increased  $G_F^{355}$  values are observed during the period from March to  
 375 October, indicating enhanced concentrations of fluorescent aerosol components. This seasonal increase is attributed to the  
 376 presence of aerosol mixtures influenced by both pollen emissions and biomass-burning aerosols. Especially, during the summer  
 377 months (i.e., June–August), higher values in  $G_F^{355}$  are evident, consistent with the frequent occurrence of smoke aerosols  
 378 originating from regional wildfires in Greece or the Balkans as well as long-range transported biomass-burning plumes from  
 379 North America (e.g., Canada), that are detected not only within the boundary layer but also at higher altitudes.

380



381



382 **Figure 6. Vertical distribution of aerosol layers observed by THELISYS from April 2024 until December 2025. (a) Mean spectral**  
 383 **fluorescence capacity  $G_F^{355}$  for each detected aerosol layer, colours represent logarithmically scaled  $G_F^{355}$ -values. (b) Aerosol layer**  
 384 **classification based mainly on spectral fluorescence capacity, with colours indicating the aerosol type. The vertical extent of each**  
 385 **band denotes the base and top altitude of the detected layer. Blue hatched layers correspond to mixed pollen aerosol layers, for**  
 386 **which the classification is considered less certain and remains under investigation compared to other aerosol types (the same applies**  
 387 **to other figures).**

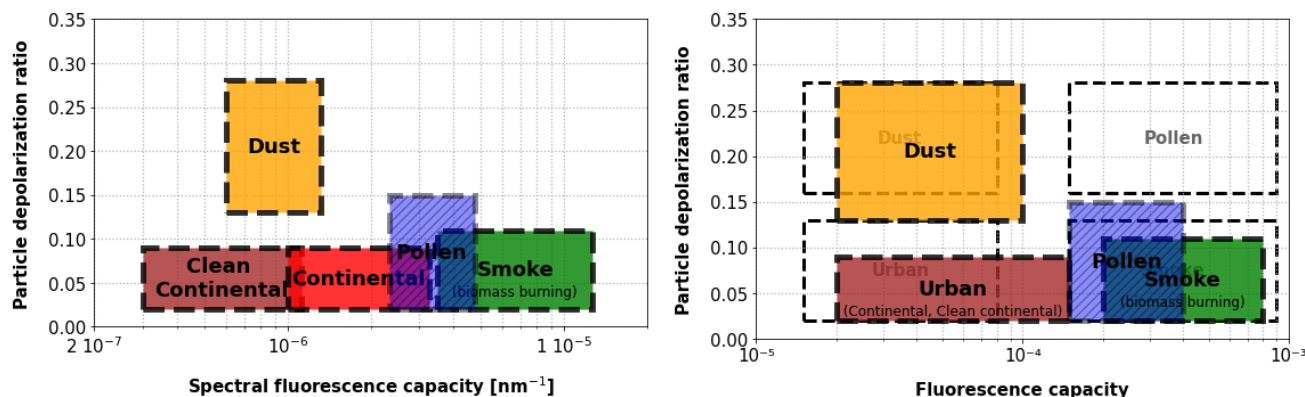
388 Based on the analysis of 50 cases of fluorescence lidar measurements obtained by THELISYS, Fig. 7 and Table 8, summarize  
 389 the aerosol typing framework adopted in this study that relies on the combined use of spectral fluorescence capacity, with IF  
 390 with IF center wavelengths of either 466 nm or 470 nm, and the particle linear depolarization ratio at 532 nm. Dust particles  
 391 are characterized by low spectral fluorescence capacity and high depolarization ratios, which is consistent with their non-  
 392 spherical mineral nature. Smoke aerosols exhibit significantly enhanced spectral fluorescence capacity combined with low  
 393 depolarization values, reflecting the presence of biomass-burning particles at high altitudes during the summer months. Pollen  
 394 particles exhibit a fairly high spectral fluorescence capacity with relatively low depolarization, supporting their identification  
 395 primarily at lower to mid-tropospheric altitudes during the pollen season It is important to note that their characterization is  
 396 complicated by the fact that pollen particles frequently occur as part of mixed aerosol layers, often combined with urban,  
 397 smoke or other aerosol types. Moreover, the particle linear depolarization ratio of pollen strongly depends on the dominant  
 398 pollen taxa, which varies with geographic region and season, leading to additional variability in the observed optical properties.  
 399 Continental aerosols show lower spectral fluorescence capacity and depolarization ratios compared to smoke and dust,  
 400 indicating weaker fluorescent and small particles, which are typically confined to the lower atmospheric layers.

402 **Table 8. Characteristic ranges of layer mean spectral fluorescence capacity ( $G_F^{355}$ ) and particle linear depolarization ratio (PLDR<sub>532</sub>)**  
 403 **for selected aerosol types**

Aerosol type	$G_F^{355}$ ( $10^{-6} \text{ nm}^{-1}$ )		PLDR <sub>532</sub>	
	Minimum value	Maximum value	Minimum value	Maximum value
Smoke	3.5	12.7	0.02	0.11
Dust	0.6	1.3	0.10	0.28
Pollen	2.3	4.8	0.02	0.14
Continental	1.0	3.3	0.02	0.08
Clean continental	0.3	1.2	0.02	0.08

404

405



406

407

408

Figure 7. (a) Aerosol typing in Thessaloniki based on spectral fluorescence capacity and particle depolarization ratio and (b) based on fluorescence capacity and particle depolarization ratio. Dashed boxes show results of Veselovskii et. al. (2022b).

409

### 3.4.2 Comparison of aerosol typing methods

410

411

412

413

414

415

416

417

418

419

420

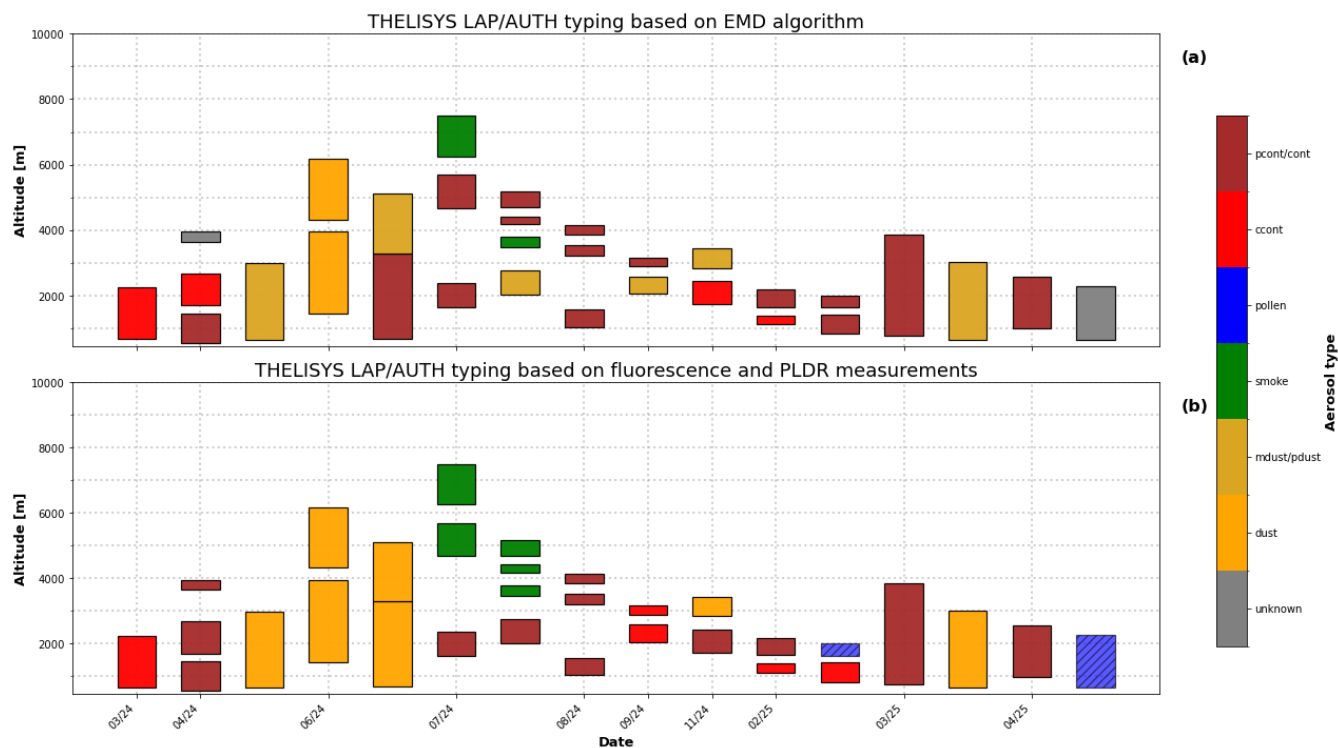
421

422

423

The THELISYS lidar sub-dataset covering March 2024 to April 2025 was analysed for aerosol typing using both the EMD and the fluorescence capacity classification. For the 16 cases, 31 layers are identified by the WCT and all of them are above 350 m, as previously. EMD classified 29 layers (93%), and 2 layers (7%) were not assigned to any cluster (the Mahalanobis distance values larger than 5), showing an overall higher identification rate. Figure 8 presents the vertical distribution and temporal evolution of the aerosol layer types detected over Thessaloniki area. Across this period, layers are observed from near the surface up to approximately 8 km, indicating the presence of both boundary layer aerosols and elevated free-tropospheric layers. The dominant aerosol categories include dust and mixed/polluted dust (orange and dark orange), smoke (green), pollen (blue), clean continental (red), polluted continental (brown), and a small number of unclassified or unknown layers (grey), as inferred from the application of both EMD and fluorescence based aerosol typing.

From this dataset, it is evident that altitude layers below 2 km are dominated by clean and polluted continental aerosols, reflecting local and regional sources, while higher altitude layers are more frequently classified as dust, mixed dust, or smoke, indicating long-range transport processes. The highest altitude layers, occasionally extending beyond 8–9 km, are predominantly classified as polluted continental or smoke, especially in the EMD classification.

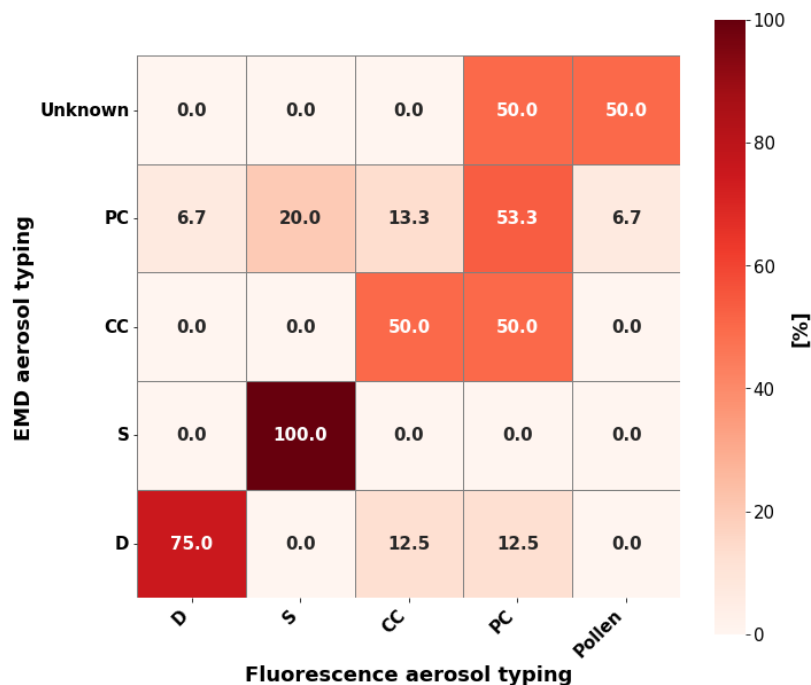


424

425

Figure 8. Vertical aerosol classification derived from (a) EMD, or (b) fluorescence properties.

426



427

428 **Figure 9. Confusion matrix between EMD (truth) and fluorescence aerosol typing (prediction).**

429 Figure 9 illustrates the overall differences in aerosol typing within the THELISYS dataset that emerge from the comparison of  
 430 the two classification approaches. We considered the EMD output as the reference in our study because EMD has previously  
 431 been applied in EARLINET dataset and been validated as a reliable method for typing (Voudouri et al., 2019; Mylonaki et al.,  
 432 2021). Thus, each row is normalized by the total number of components identified by the EMD algorithm. Dust and mixed-  
 433 dust layers (summarized as ‘dust’ in Fig. 9) are consistently detected by both methods (75% agreement), as the particle  
 434 depolarization ratio plays a critical role in the separation of dust aerosols. A similarly high agreement is observed for smoke  
 435 aerosols, with all EMD classified smoke layers assigned to the smoke fluorescence category. However, the number of smoke  
 436 cases in the dataset is limited. For polluted continental aerosols, a partial agreement (53.3%) is found between the two methods.  
 437 The EMD classification overlaps with multiple fluorescence categories (e.g. smoke 20%) suggesting that the spectral  
 438 fluorescence capacity is a very useful parameter especially for the separation between smoke and polluted continental aerosols,  
 439 as smoke is a highly fluorescing aerosol compared to others. Clean continental aerosols exhibit a lower agreement (50%), with  
 440 difficulty in separation of polluted and clean continental aerosols. This separation based on their fluorescence capacity values  
 441 is at an initial stage of analysis and remains under investigation. The same applies to pollen detection. In the present dataset,  
 442 only two mixed pollen layers were identified based on high fluorescence capacity values. Of these, one was classified as  
 443 polluted continental by the EMD method, while the other remained unclassified. Mixed pollen layers are also under  
 444 investigation and represent a promising opportunity for further development of aerosol typing algorithms.



445 We conclude that fluorescence typing could help in clearer separation between dust, smoke and mixed pollen layers. Overall,  
446 the comparison makes their combined use valuable for a more accurate characterization of aerosol vertical structure and source  
447 attribution.

#### 448 **4. Conclusion**

449 In this study, fluorescence lidar observations from the upgraded THELISYS system were used to investigate aerosol typing  
450 over Thessaloniki, an urban site strongly influenced by a wide range of natural and anthropogenic aerosol sources. The detected  
451 aerosol layers were classified, for the first time, using both the spectral fluorescence capacity and the particle depolarization  
452 ratio, and were further intercompared with a conventional lidar derived optical properties classification scheme, developed  
453 within EARLINET.

454 Case studies of long-range transported biomass-burning smoke, Saharan dust intrusions, and mixed pollen layers highlighted  
455 the added value of fluorescence measurements in discriminating between these and polluted continental aerosols. Dust layers  
456 consistently exhibited low spectral fluorescence capacity and high depolarization ratios, while mixed pollen layers showed  
457 enhanced spectral fluorescence capacity at lower altitudes ( $>2 \times 10^{-6} \text{ nm}^{-1}$ ), reflecting the biological origin of the particles. These  
458 results confirm that spectral fluorescence capacity could provide complementary information for aerosol typing.

459 The analysis of a larger THELISYS dataset spanning more than one year of measurements revealed clear seasonal and vertical  
460 patterns in spectral fluorescence capacity. High values (greater than  $3.6 \times 10^{-6} \text{ nm}^{-1}$ ) were predominantly observed during the  
461 summer months and at elevated altitudes, associated with biomass-burning smoke, whereas values around unity occurred  
462 throughout the year, mainly within the boundary layer. Low spectral fluorescence capacity ( $<1 \times 10^{-6} \text{ nm}^{-1}$ ) values were linked  
463 to dust events.

464 Overall, this work demonstrates that the integration of fluorescence measurements into operational Raman lidar systems  
465 significantly improves the aerosol classification, particularly in complex environments such as the Eastern Mediterranean. The  
466 results support the future inclusion of spectral fluorescence capacity as a standard intensive parameter within EARLINET and  
467 ACTRIS frameworks and underline the need for harmonized fluorescence retrievals across the different lidar configurations.  
468 Future work will focus on expanding the statistical basis of the dataset, refining mixed-aerosol classification, and exploiting  
469 spectral fluorescence information to further enhance aerosol source attribution.

#### 470 **Data availability.**

471 Lidar data and products are available upon request at [balis@auth.gr](mailto:balis@auth.gr). The backward trajectory analysis is based on air mass  
472 transport computation with the NOAA (National Oceanic and Atmospheric Administration) HYSPLIT model (available  
473 online: <https://www.ready.noaa.gov/HYSPLIT.php>, last access: 29 January 2026).



474 **Author contributions.**

475 GP processed the data and wrote the manuscript. KV processed the data for the EMD algorithm. KM contributed to the aerosol  
476 identification using the WCT method, and PP contributed to the development of the fluorescence retrieval algorithm. NS and  
477 JR contributed to the comparison of different fluorescence interference filters. DB is the PI of Thessaloniki EARLINET station.  
478 All co-authors participated in discussions on the results and contributed to proofreading the manuscript.

479 **Competing interests.**

480 The contact author has declared that none of the authors has any competing interests.

481 **Acknowledgements**

482 Part of this work was supported by the COST Action EARLICOST (CA24135), supported by COST (European Cooperation  
483 in Science and Technology).

484 **References**

- 485 Ansmann A., Riebesell M., and Claus Weitkamp C.: Measurement of atmospheric aerosol extinction profiles with a Raman  
486 lidar., *Opt. Lett.* 15, 746-748 , <https://doi.org/10.1364/OL.15.000746>, 1990.
- 487 Baars, H., Ansmann, A., Engelmann, R., and Althausen, D.: Continuous monitoring of the boundary-layer top with lidar,  
488 *Atmos. Chem. Phys.*, 8, 7281–7296, <https://doi.org/10.5194/acp-8-7281-2008>, 2008.
- 489 Brooks, I. M.: Finding Boundary Layer Top: Application of a Wavelet Covariance Transform to Lidar Backscatter Profiles, *J.*  
490 *Atmos. Ocean. Tech.*, 20, 1092–1105, [https://doi.org/10.1175/1520-0426\(2003\)020<1092:FBLTAO>2.0.CO;2](https://doi.org/10.1175/1520-0426(2003)020<1092:FBLTAO>2.0.CO;2), 2003.
- 491 Burton, S. P., Hair, J. W., Kahnert, M., Ferrare, R. A., Hostetler, C. A., Cook, A. L., Harper, D. B., Berkoff, T. A., Seaman, S.  
492 T., Collins, J. E., Fenn, M. A., and Rogers, R. R.: Observations of the spectral dependence of linear particle depolarization  
493 ratio of aerosols using NASA Langley airborne High Spectral Resolution Lidar, *Atmos. Chem. Phys.*, 15, 13453–13473,  
494 <https://doi.org/10.5194/acp-15-13453-2015>, 2015.
- 495 Charalampopoulos, A., Damialis, A., Lazarina, M., Halley, J.M., and Vokou, D.: Spatiotemporal Assessment of Airborne  
496 Pollen in the Urban Environment: The Pollenscape of Thessaloniki as a Case Study. *Atmos. Environ.*, 247, 118185,  
497 [doi:10.1016/j.atmosenv.2021.118185](https://doi.org/10.1016/j.atmosenv.2021.118185), 2021.
- 498 D'Amico, G., Amodeo, A., Baars, H., Binietoglou, I., Freudenthaler, V., Mattis, I., Wandinger, U., and Pappalardo, G.:  
499 EARLINET Single Calculus Chain – overview on methodology and strategy, *Atmos. Meas. Tech.*, 8, 4891–4916,  
500 <https://doi.org/10.5194/amt-8-4891-2015>, 2015.



- 501 Damialis, A., Halley, J.M., Gioulekas, D., and Vokou, D.: Long-Term Trends in Atmospheric Pollen Levels in the City of  
502 Thessaloniki, Greece. *Atmos. Environ.*, 41, 7011–7021, doi:10.1016/j.atmosenv.2007.05.009, 2007.
- 503 Damialis, A., Kaimakamis, E., Konoglou, M., Akritidis, I., Traidl-Hoffmann, C., and Gioulekas, D.: Estimating the Abundance  
504 of Airborne Pollen and Fungal Spores at Variable Elevations Using an Aircraft: How High Can They Fly? *Sci. Rep.*, 7, 1–11,  
505 doi:10.1038/srep44535, 2017.
- 506 EARLINET: A European Aerosol Research Lidar Network to Establish an Aerosol Climatology, <https://www.earlinet.eu>,  
507 2000.
- 508 Fernald F. G.: Analysis of atmospheric lidar observations: some comments, *Appl. Opt.* 23, 652–653,  
509 <https://doi.org/10.1364/AO.23.000652>, 1984.
- 510 Ferrare, R. A., Melfi, S. H., Whiteman, D. N., Evans, K. D., and Leifer, R.: Raman lidar measurements of aerosol extinction  
511 and backscattering: 1. Methods and comparisons, *J. Geophys. Res.*, 103, 19663–19672, 1998.
- 512 Filioglou, M., Leskinen, A., Vakkari, V., O'Connor, E., Tuononen, M., Tuominen, P., Laukkanen, S., Toiviainen, L., Saarto,  
513 A., Shang, X., Tiitta, P., and Komppula, M.: Spectral dependence of birch and pine pollen optical properties using a synergy  
514 of lidar instruments, *Atmos. Chem. Phys.*, 23, 9009–9021, <https://doi.org/10.5194/acp-23-9009-2023>, 2023.
- 515 Freudenthaler, V., Linné, H., Chaikovski, A., Rabus, D., and Groß, S.: EARLINET lidar quality assurance tools, *Atmos. Meas.*  
516 *Tech. Discuss.* [preprint], <https://doi.org/10.5194/amt-2017-395>, in review, 2018.
- 517 Gast, B., Jimenez, C., Ansmann, A., Haarig, M., Engelmann, R., Fritzsche, F., Floutsi, A. A., Griesche, H., Ohneiser, K., Hofer,  
518 J., Radenz, M., Baars, H., Seifert, P., and Wandinger, U.: Invisible aerosol layers: improved lidar detection capabilities by  
519 means of laser-induced aerosol fluorescence, *Atmos. Chem. Phys.*, 25, 3995–4011, <https://doi.org/10.5194/acp-25-3995-2025>,  
520 2025.
- 521 Gidarakou, M., Papayannis, A., Gao, K., Gidarakos, P., Crouzy, B., Foskinis, R., Erb, S., Brem, B. T., Zhang, C., Lieberherr,  
522 G., Collaud Coen, M., Sikoparija, B., Kanji, Z. A., Clot, B., Calpini, B., Giagka, E., and Nenes, A.: Profiling pollen and  
523 biomass burning particles over Payerne, Switzerland using laser-induced fluorescence lidar and in situ techniques during the  
524 2023 PERICLES campaign, *Atmos. Chem. Phys.*, 26, 923–945, <https://doi.org/10.5194/acp-26-923-2026>, 2026.
- 525 Gioulekas, D., Papakosta, D., Damialis, A., Spieksma, F., Giouleka, P., Patakas, D.: Allergenic Pollen Records (15 Years) and  
526 Sensitization in Patients with Respiratory Allergy in Thessaloniki, Greece. *Allergy* 2004, 59, 174–184, doi:10.1046/J.1398-  
527 9995.2003.00312.X, 2004.
- 528 Hu, Q., Goloub, P., Veselovskii, I., and Podvin, T.: The characterization of long-range transported North American biomass  
529 burning plumes: what can a multi-wavelength Mie–Raman-polarization fluorescence lidar provide?, *Atmos. Chem. Phys.*, 22,  
530 53995414, <https://doi.org/10.5194/acp-22-5399-2022>, 2022.
- 531 HYSPLIT: HYbrid Single-Particle Lagrangian Integrated Trajectory model, backward trajectory calculation tool, [https://www.  
532 ready.noaa.gov/hypub-bin/trajtype.pl?runtype=archive](https://www.ready.noaa.gov/hypub-bin/trajtype.pl?runtype=archive) (last access: 29 January 2026), 2026.
- 533 Klett, J. D.: Stable analytical inversion solution for processing lidar returns, *Appl. Optics*, 20, 211–220,  
534 <https://doi.org/10.1364/AO.20.000211>, 1981.



- 535 Klett, J. D.: Lidar inversion with variable backscatter/extinction ratios, *Appl. Optics*, 24, 1638–1643, 1985.
- 536 Komnos I., Michali M., Ziavra N., Katotomichelakis M., Kastanioudakis I.: A Study of Airborne Pollen Grains and Fungal  
537 Spores in the Region of Epirus (Northwestern Greece). *Cureus* 14(6): e26335. doi:10.7759/cureus.26335, 2022.
- 538 Mahalanobis, P. C.: On the generalized distance in statistics, in: *Proceedings of the National Institute of Science of India*, 49–  
539 55, 1936.
- 540 Michailidis K., “Optical and microphysical properties of atmospheric aerosols based on ground-based and satellite remote  
541 sensing techniques” (2023)
- 542 Michailidis K., Garane K., Karagkiozidis D., Peletidou G., Voudouri K.A., Balis D., Bais A.: Extreme wildfires over northern  
543 Greece during summer 2023 – Part A: Effects on aerosol optical properties and solar UV radiation. *Atmospheric Research*,  
544 Volume 311, 107700, ISSN 0169-8095, <https://doi.org/10.1016/j.atmosres.2024.107700>, 2024.
- 545 Mylonaki, M., Giannakaki, E., Papayannis, A., Papanikolaou, C.-A., Komppula, M., Nicolae, D., Papagiannopoulos, N.,  
546 Amodeo, A., Baars, H., and Soupiona, O.: Aerosol type classification analysis using EARLINET multiwavelength and  
547 depolarization lidar observations, *Atmos. Chem. Phys.*, 21, 2211–2227, <https://doi.org/10.5194/acp-21-2211-2021>, 2021.
- 548 Nickovic S, Kallos G, Papadopoulos A, Kakaliagou O. A model for prediction of desert dust cycle in the atmosphere. *J.*  
549 *Geophys. Res.* 2001; 106: 18113–18130. 10.3402/tellusb.v64i0.18539.
- 550 Papadogiannaki, S., Karatzas, K., Kontos, S., Poupkou, A., Melas, D.: A Multi-Model Approach to Pollen Season Estimations:  
551 Case Study for Olea and Quercus in Thessaloniki, Greece. *Atmosphere*, 16, 454. <https://doi.org/10.3390/atmos16040454>,  
552 2025.
- 553 Papagiannopoulos, N., Mona, L., Amodeo, A., D'Amico, G., Gumà Claramunt, P., Pappalardo, G., Alados-Arboledas, L.,  
554 Guerrero-Rascado, J. L., Amiridis, V., Kokkalis, P., Apituley, A., Baars, H., Schwarz, A., Wandinger, U., Biniotoglou, I.,  
555 Paschalidou, A.K., Psistaki, K., Charalampopoulos, A., Vokou, D., Kassomenos, P., Damialis, A.: Identifying Patterns of  
556 Airborne Pollen Distribution Using a Synoptic Climatology Approach. *Sci. Total Environ.*, 714, 136625,  
557 doi:10.1016/j.scitotenv.2020.136625, 2020.
- 558 Paschou, P., Siomos, N., Tsekeri, A., Louridas, A., Georgoussis, G., Freudenthaler, V., Biniotoglou, I., Tsaknakis, G.,  
559 Tavernarakis, A., Evangelatos, C., von Bismarck, J., Kanitz, T., Meleti, C., Marinou, E., and Amiridis, V.: The eVe reference  
560 polarisation lidar system for the calibration and validation of the Aeolus L2A product, *Atmos. Meas. Tech.*, 15, 2299–2323,  
561 <https://doi.org/10.5194/amt-15-2299-2022>, 2022.
- 562 Reichardt, J.: Cloud and Aerosol Spectroscopy with Raman Lidar, *J. Atmo. Ocean. Tech.*, 31, 1946–1963,  
563 <https://doi.org/10.1175/JTECH-D-13-00188.1>, 2014.
- 564 Reichardt, J., Leinweber, R., and Schwebe, A.: Fluorescing aerosols and clouds: investigations of co-existence, *EPJ Web*  
565 *Conf.*, 176, 05010, <https://doi.org/10.1051/epjconf/201817605010>, 2018.
- 566 Reichardt, J., Behrendt, O., and Lauer mann, F.: Spectrometric fluorescence and Raman lidar: absolute calibration of aerosol  
567 fluorescence spectra and fluorescence correction of humidity measurements, *Atmos. Meas. Tech.*, 16, 1–13,  
568 <https://doi.org/10.5194/amt-16-1-2023>, 2023.



- 569 Reichardt, J., Lauer mann, F., and Behrendt, O.: Aerosol studies with spectrometric fluorescence and Raman lidar, in:  
570 Proceedings of the 30th International Laser Radar Conference, edited by: Sullivan, J. T., Leblanc, T., Tucker, S., Demoz, B.,  
571 Eloranta, E., Hostetler, C., Ishii, S., Mona, L., Moshary, F., Papayannis, A., and Rupavatharam, K., Springer International  
572 Publishing, Cham, 279–285, ISBN 978-3-031-37818-8, 2023b.
- 573 Reichardt, J., Lauer mann, F., and Behrendt, O.: Fluorescence spectra of atmospheric aerosols, *Atmos. Chem. Phys.*, 25, 5857–  
574 5892, <https://doi.org/10.5194/acp-25-5857-2025>, 2025.
- 575 Saito, Y., Ichihara, K., Morishita, K., Uchiyama, K., Kobayashi, F., and Tomida, T.: Remote Detection of the Fluorescence  
576 Spectrum of Natural Pollens Floating in the Atmosphere Using a Laser Induced Fluorescence Spectrum (LIFS) Lidar, *Remote  
577 Sens. Basel*, 10, 1533, <https://doi.org/10.3390/rs10101533>, 2018.
- 578 Sassen, K.: Polarization in Lidar, in: *Lidar: Range-Resolved Optical Remote Sensing of the Atmosphere*, edited by: Weitkamp,  
579 C., Springer New York, New York, NY, 19–42, [https://doi.org/10.1007/0-387-25101-4\\_2](https://doi.org/10.1007/0-387-25101-4_2), 2005.
- 580 Siomos, N., Balis, D. S., Poupkou, A., Liora, N., Dimopoulos, S., Melas, D., Giannakaki, E., Filioglou, M., Basart, S., and  
581 Chaikovsky, A.: Investigating the quality of modeled aerosol profiles based on combined lidar and sunphotometer data, *Atmos.  
582 Chem. Phys.*, 17, 7003–7023, <https://doi.org/10.5194/acp-17-7003-2017>, 2017.
- 583 Siomos, N., Balis, D. S., Voudouri, K. A., Giannakaki, E., Filioglou, M., Amiridis, V., Papayannis, A., and Fragkos, K.: Are  
584 EARLINET and AERONET climatologies consistent? The case of Thessaloniki, Greece, *Atmos. Chem. Phys.*, 18, 11885–  
585 11903, <https://doi.org/10.5194/acp-18-11885-2018>, 2018.
- 586 Stein, A. F., Draxler, R. R., Rolph, G. D., Stunder, B. J. B., Cohen, M. D., and Ngan, F.: NOAA's hysplit atmospheric transport  
587 and dispersion modeling system, *B. Am. Meteorol. Soc.*, 96, 2059–2077, <https://doi.org/10.1175/BAMS-D-14-00110.1>, 2015  
588 (data available at: <https://www.ready.noaa.gov/HYSPLIT.php>, last access: 29 January 2026).
- 589 Venable D. D., Whiteman D. N., Calhoun M. N., Dirisu A. O., Connell R. M., Landulfo E.: Lamp mapping technique for  
590 independent determination of the water vapor mixing ratio calibration factor for a Raman lidar system, *Appl. Opt.* 50, 4622–  
591 4632, 2011.
- 592 Veselovskii, I., Hu, Q., Goloub, P., Podvin, T., Korenskiy, M., Pujol, O., Dubovik, O., and Lopatin, A.: Combined use of Mie  
593 Raman and fluorescence lidar observations for improving aerosol characterization: feasibility experiment, *Atmos. Meas. Tech.*,  
594 13, 6691–6701, <https://doi.org/10.5194/amt-13-6691-2020>, 2020.
- 595 Veselovskii, I., Hu, Q., Goloub, P., Podvin, T., Choël, M., Visez, N., and Korenskiy, M.: Mie–Raman–fluorescence lidar  
596 observations of aerosols during pollen season in the north of France, *Atmos. Meas. Tech.*, 14, 4773–4786,  
597 <https://doi.org/10.5194/amt14-4773-2021>, 2021.
- 598 Veselovskii, I., Hu, Q., Ansmann, A., Goloub, P., Podvin, T., and Korenskiy, M.: Fluorescence lidar observations of wildfire  
599 smoke inside cirrus: a contribution to smoke–cirrus interaction research, *Atmos. Chem. Phys.*, 22, 5209–5221,  
600 <https://doi.org/10.5194/acp-22-5209-2022>, 2022a.



- 601 Veselovskii, I., Hu, Q., Goloub, P., Podvin, T., Barchunov, B., and Korenskii, M.: Combining Mie–Raman and fluorescence  
602 observations: a step forward in aerosol classification with lidar technology, *Atmos. Meas. Tech.*, 15, 4881–4900,  
603 <https://doi.org/10.5194/amt-15-4881-2022>, 2022b.
- 604 Veselovskii, I., Kasianik, N., Korenskii, M., Hu, Q., Goloub, P., Podvin, T., and Liu, D.: Multiwavelength fluorescence lidar  
605 observations of smoke plumes, *Atmos. Meas. Tech.*, 16, 20552065, <https://doi.org/10.5194/amt-16-2055-2023>, 2023.
- 606 Veselovskii, I., Hu, Q., Goloub, P., Podvin, T., Dubois, G., Kolgotin, A., and Korenskii, M.: Impact of water uptake on  
607 fluorescence of atmospheric aerosols: insights from Mie–Raman–fluorescence lidar measurements, *Atmos. Meas. Tech.*, 18,  
608 6039–6051, <https://doi.org/10.5194/amt-18-6039-2025>, 2025.
- 609 Vokou, D., Charalampopoulos, A., Lazarina, M., Tsingani-Papanikolaou, O., Leontidou, K., Paschalidou, D., Damialis, A.,  
610 Hanlidou, E.: Plants on the Ground, Pollen in the Air: How Much Do They Match? *Aerobiologia (Bologna)*, 40, 485–499,  
611 doi:10.1007/s10453-024-09838-6, 2024.
- 612 Voudouri, K. A., Siomos, N., Michailidis, K., Papagiannopoulos, N., Mona, L., Cornacchia, C., Nicolae, D., and Balis, D.:  
613 Comparison of two automated aerosol typing methods and their application to an EARLINET station, *Atmos. Chem. Phys.*,  
614 19, 10961–10980, <https://doi.org/10.5194/acp-19-10961-2019>, 2019.
- 615 Voudouri, K. A., Siomos, N., Michailidis, K., D’Amico, G., Mattis, I., & Balis, D.: Consistency of the Single Calculus Chain  
616 Optical Products with Archived Measurements from an EARLINET Lidar Station. *Remote Sensing*, 12(23), 3969.  
617 <https://doi.org/10.3390/rs12233969>, 2020.
- 618 Whiteman D. N.: Examination of the traditional Raman lidar technique. II. Evaluating the ratios for water vapor and aerosols,  
619 *Appl. Opt.* 42, 2593–2608, <https://doi.org/10.1364/AO.42.002593>, 2003.